ORIGINAL ARTICLE

A new resonance-based design approach to reduce motor torque requirements in automated machinery

Luca Luzi[1] · Amedeo Carloni[2] · Eugenio Monari[2] · Giovanni Berselli[3] · Rocco Vertechy[2]

Abstract

In the last decades, compliant mechanisms have been widely studied but their application has not been widespread due to their susceptibility to fatigue and the lack of systematic design methodologies. In this paper, the authors propose a new approach to be used in the automated machinery mechanism design (the mechanisms are usually subjected to predominant inertial loads) that exploits the capability of the compliant joints to store and release elastic energy in order to reduce the motor torque requirements. Thanks to the carbon-fiber reinforced 3D printing technologies, the compliant joint stiffness can be properly designed to obtain, for the considered mechanism, a resonant condition during its nominal functioning. Moreover, topology optimization can be successfully employed to reduce the mechanism component inertia (keeping the same overall mechanism stiffness) and thus, further diminish the torque requirements. In order to assess the quality of the proposed approach, a pusher mechanism used in a real automated machine has been considered. A prototype has been manufactured to evaluate the effect of the compliant joint introduction and the topology optimization on the motor torque reduction. To validate the results, an experimental campaign has been conducted. Comparison between the standard design approach and the new one emphasizes the superior contribution of compliant joint introduction on the motor torque reduction: a 97% and 96% reduction on the RMS and peak motor torque, respectively, is achieved resorting to the new design approach. Although a high repeatability is achieved, a slight deviation of the trajectory with respect to the ideal one is however registered.

Keywords Additive manufacturing · Continuous fibre reinforced thermoplastics · Size optimization · Topology optimization

✉ Giovanni Berselli
giovanni.berselli@unige.it

Luca Luzi
luca.luzi@univr.it

Amedeo Carloni
amedeo.carloni@studio.unibo.it

Eugenio Monari
eugenio.monari3@unibo.it

Rocco Vertechy
rocco.vertechy@unibo.it

1 Department of Computer Science, University of Verona, Ca'
   Vignal 2 - Strada Le Grazie, 15, 37134 Verona, Italy

2 Department of Industrial Engineering, Alma Mater
   Studiorum - University of Bologna, Viale Risorgimento, 2,
   40136 Bologna, Italy

3 Department of Mechanics, Energetics, Management
   and Transportation, University of Genova, Via All'Opera Pia,
   15, 16146 Genoa, Italy

1 Introduction

The computational design development of the last decades has significantly affected the engineering world. Computer-aided design (CAD) and computer-aided engineering (CAE) are essential tools at the designer disposal to develop new products [1]: CAD provides a very efficient parametric geometry visualization, accelerating the process from the conceptual idea to the manufacturing process; CAE technologies can accurately predict product future performances and support the engineers throughout the design process [2]. CAE simulations are useful, for example, to analyse the kinematics and dynamics of a mechanical system (i.e. multibody analysis, MBD), minimize its overall dimension and weight checking deformation and stresses during its nominal functioning condition (i.e. finite element (FE) analysis), as well as to simulate and optimize the actuation system performance. Moreover, several design variants can be evaluated in a reduced time [2, 3] and thus, physical testing stage can

be focused on the validation of a system already optimized and tested in simulation with obvious advantages in terms of cost saving. A variety of CAD and CAE software is commercially available (*PTC Creo*, *SolidWorks*, *Catia*, and *Siemens NX* are some of the most popular CAD, whereas *Ansys*, *Abaqus MSC Marc*, and *Adams* are some of the most popular CAE software), although most of them are either CAD or CAE tools so that the designer has to work with two separate software. Many efforts have been made over the past years to create reliable procedures [4–15] to exchange data from one software to another mostly based on the use of standard file formats (e.g. STEP). However, some issues related to information loss and compatibility remain with these techniques. Lately, even though some CAD/CAE combinations can be found to work efficiently (e.g., data sharing between *PTC Creo* and *Ansys* [16, 17], and parametric optimization performed with the mutual contribution of *Creo Parametric* and *Ansys* [18, 19]) the industrial world is headed towards the use of a unique software that is capable to share information among several interconnected modules. Although in some cases the CAD/CAE unique software proved to be very efficient and easy to use [1, 20], it is not the proper tool when in-depth analyses need to be performed.

Structural optimization [21–28] is the most helpful module available in the majority of CAD and CAE software at disposal of the designer, in order to maximize the mechanical component/system performance. In fact, lighter design is desirable in many industrial applications (e.g., automated machinery) to minimize the motor power consumption: in general, with structural optimization, the best structure geometry [21] can be defined that ensures both high-performance mechanical behaviour (e.g., high stiffness, low weight, and actuation torque/force) as well as low cost.

Topology and size structural optimizations are regarded as the most popular ones and special modules are typically found in some mainly CAD software (e.g., *PTC Creo*, *SolidWorks*). The usage of a particular type of structural optimization affects not only the result potentialities but also the manufacturing process needed to achieve that result. In general, it is common to find applications of topology optimization (TO) in combination with additive manufacturing technologies (AMT) [29–31] (also known as 3D printing) rather than with material subtractive technologies (MST) [32]. Instead, size optimization (SO) can be successfully applied with MST. Topology optimization is a FE-based method that aims to determine how to place material within a prescribed design domain, in order to obtain the best structural performance. Several approaches have been proposed during the past 20 years: the most representative are the density approach [33–35] (also known as the simplified isotropic material with penalization SIMP) and the level-set one [36–39] (an exhaustive review on the TO approaches can be found in [40]). In the first one, given a predefined amount of material, a pseudo-density (0–1; 0 is a hole, 1 is an active element) is assigned as a design variable to each finite element. Successively, a global penalty parameter is added to weight of the pseudo-density in order to transform the discrete optimization problem into a continuous one. Since this method suffers from a poor defined boundary [41], the interpretation of the designer is needed: manual interventions are needed to produce a CAD model, and this process is time consuming and labour intensive [42]). For this reason, the level-set approach aims directly at pushing the shape boundary instead of handling the FEs, avoiding ambiguous and irregular design. The often-complex shapes resulting from TO do not suit the MST manufacturing capability (also with casting, typical hollow, and framework-like structures make TO difficult in practice, and many modifications must be done to create a feasible design [43]). Instead, the AMT enables to overcome the MST limits making the fabrication of complex geometrical features possible [41, 44–49] since parts can be built via joining material layer by layer. On the other hand, the key limitations of the AMT include relatively high expense and relatively small build volumes [50].

In the size optimization problem, typically the member cross-sectional dimensions (thickness or width) of a component are treated as design variables. Its applicability to MST (and thus, high-volume production), in combination with the capability to reach a reliable result quickly and with a unique CAD/CAE software make SO the preferred choice in the industrial field with respect to TO.

Over the past 30 years, AMT has undergone a very rapid growth [51]. Early AMT applications focused on models and prototypes [52] and successively on the production of rapid and soft tooling (e.g., vacuum and silicone casting moulds) [53]. Nowadays, it is also used to produce finished parts (especially when a high level of customization is needed). Lately, fuse filament deposition modelling (FDM) technique [54–58] (a specific type of AMT technique) is receiving great attention thanks to its capability to insert reinforcing fibres into a thermoplastic matrix improving the mechanical characteristics of the plastic parts [59–61]: the thermoplastic matrix merges and protects the fibres that support the load. Continuous fibre-reinforced polymer (FRP) composites have been used for many applications (e.g., aerospace and automotive) to create strong yet lightweight products due to their high strength-to-weight and stiffness-to-weight ratios. Reinforced polymeric components with a strength and elasticity modulus comparable to those made of aluminium alloy (tensile strength is observed to be higher [62]), mostly used in the automated machinery, can be obtained without significantly increasing their weight. Moreover, a particular arrangement of the fibres can be found to obtain a desired orthotropic material behaviour [49, 63–69]. For example, the tensile and flexural behaviour of a lamina in which the fibres are deposited along the longitudinal direction change

according to the distance of the fibres to the neutral axis and to the number of the fibres deposited. The capability of FDM to create high-performance orthotropic polymeric material can be effectively applied to the realization of compliant joints (CJs) [31, 70, 71]. CJs [70, 72–74], which are connectors that, thanks to their deformation, provide relative motion among the connected parts. When compared to traditional kinematic pairs, several benefits come from the use of CJs in mechanism design [75, 76]: reduced part count, less friction, absence of wear and back-lash, light weight, low cost, and fine motion. Moreover, CJs can store elastic energy and release it when needed. They are widely used in several applications (e.g. robotic system [77–79], MEMS devices [80], precision engineering [81], dielectric-elastomer actuators [82], surgical robot [83, 84] and sensors [85]). However, two main limitations restrain the spreading of CJ: (i) in repetitive motions, the joints may be prone to high stress concentrations and hence a poor fatigue life [74]; (ii) in applications where compressive forces are present, CJ may be affected by buckling failure [86]. In both cases, increasing their thickness can lead to an undesired stiffness and dimension (while preserving their flexibility) that might force to oversize the actuation system. These drawbacks can be overcome with the CFT-FDM technology that is able to realize orthotropic CJs and, thus, tune their stiffness along every direction according to the load condition. Two approaches are commonly used to address the kinestotatic analysis of mechanical systems employing CJ (usually called compliant mechanisms): FE analysis (FEA) [87] and pseudo-rigid-body (PRB) modelling [88, 89]. The FEA method is computationally expensive when only a result with acceptable accuracy is required. PRB modelling, on the other hand, is very efficient in predicting the kinetostatic behaviour of compliant mechanisms with moderate accuracy [72] (within 5% of the desired motion trajectory). Nonetheless, other methods (such as the chained-beam-constraint model (CBCM)) [90, 91], the 2R PRB model [92], the 3R PRB model [93], and the dynamic PRB model [94]) have been recently proposed in the literature to predict more efficiently the kinetostatic and dynamic performance of compliant mechanisms.

Building upon these introductory considerations, this paper presents a new design approach for compliant mechanisms employing flexible lamina, that undergo cyclic motions and are subjected to predominantly inertial loads (typical of automated machinery). In particular, SO is used to design the stiffness and the dimensions of the flexible lamina in order to make the considered mechanism work in a "resonant" condition and, thus, minimize the motor power consumption. TO is used to design mechanism components in order to minimize their inertia, thus further diminishing the motor power consumption. To evaluate the effectiveness of the presented approach, a comparison with the standard design (namely, the original design realized with SMT) is made in terms of motor torque requirements (root mean square (RMS) and peak value) and motion trajectory precision. As a case study, an existent pusher mechanism used in a pharmaceutical industry production machine is studied, tested, and redesigned according to the new CJ-AMT design method.

MarkForged MarkTwo 3D printer [95–97] has been used to manufacture the components obtained with SO and TO. The printer is provided with two nozzles: one is for the matrix deposition, the other one is for the reinforcement fibres. Two matrix materials are available: nylon and onyx (nylon with chopped carbon fibre). The following reinforcing fibres can be deposited: glass, carbon, high-strength high-temperature fiberglass, and Kevlar fibres. Among these, carbon fibres proved to yield a higher strength [62]. Two types of fibre pattern can be selected: concentric and isotropic. Concentric pattern consists of fibres deposited along the perimeter of the section. The isotropic (the term has nothing to do with the properties of the final component) pattern consists of fibres deposited along parallel lines. The isotropic pattern is observed to provide higher tensile strength and stiffness than the concentric pattern [62]. Carbon fibre reinforced onyx (CFRO) has been used for the manufacturing of the mechanism components, whereas carbon fibre reinforced nylon (CFRN; Table 1) [63–67, 98] for the flexible laminas. Moreover, to predict the lamina kinetostatic behaviour, the PRB model has been used. The results have been compared with FEA simulations and tests.

In summary, the novelty of the paper, as respect to the state-of-the art, can be described as follows: (i) results are reported quantitatively comparing the performance of a standard rigid-link mechanism, currently employed in a commercial automatic machine, and a novel solution, leveraging on the combination of large-deflection CJ, TO, and FDM printed long-fibre reinforced plastics. In particular, the paper proves that the mentioned design methods and production technology can be effectively employed in an industrial scenario; (ii) benefits in terms of motor torque reduction are highlighted, clearly showing the possibility to downsize the actuation system, with obvious benefits in terms of cost and

Table 1 Onyx and CFRN mechanical properties. The values refer to CFRO specimen with carbon fiber maximum filling level [65]

	Onyx	Nylon	CFRN[1]
ρ_{Onyx}	1200 kg/m^3	1200 kg/m^3	1400 kg/m^3
$\sigma_{\text{t,Onyx}}$	40 MPa	51 MPa	986 MPa
$E_{\text{t,Onyx}}$	2.4 GPa	1.7 GPa	62.5 GPa
$\sigma_{\text{f,Onyx}}$	71 MPa	50 MPa	485 MPa
$E_{\text{f,Onyx}}$	3 GPa	1.4 GPa	41.6 GPa
G	-	-	2.26 GPa

energy consumption; (iii) differently from the majority of partially/fully compliant mechanisms designed to operate in large deflection, the mechanism proposed here works in a "resonant" condition.

The paper is structured as follows: in Sect. 2, the original mechanism used to test the proposed approach is described; in Sect. 3, the new design procedure is explained; in Sect. 4, the experimental campaign planned to compare the design approaches is shown along with the obtained results; in Sect. 5, conclusions and future works are presented.

2 Existing mechanism

The original mechanism considered (Fig. 1) is a planar six-bar linkage Stephenson mechanism with one degree of freedom (DOF). Geometrical data are reported in Table 2. The mechanism (Fig. 2) comprises a parallelogram four-bar-linkage (links 3–6) whose coupler (link 3) is moved by an actuated crank (link 1) through a connecting rod (link 2). All the mechanism components have been made in aluminium alloy AA7075 (commercially known as ERGAL) and have been manufactured with SMT. The parallelogram four-bar-linkage architecture forces link 3 (end effector of the whole mechanism, hereinafter referred to as the slider) to translate along a circular trajectory. When numerous cycles and high velocity are considered, the use of an actual slider is usually avoided since it does not provide sufficient accuracy, and especially joint clearances may cause assembly dangerous vibrations. A Cartesian reference system is fixed to the frame, featuring: the x-axis passing through points O_2 and O_3, y-axis normal to the x-axis and passing through point O_1, z-axis chosen according to the right-hand rule. α is the angular position of the crank with respect to the x-axis. All connections between the links are made via bearings that are placed at points A-D, O_1, O_2, and O_3. The crankshaft (link 1) home position is when rockers (links 4 and 5) are in a vertical position ($\alpha = 87.15°$). The angular position α of the crankshaft is controlled by an electric motor placed in O_1. For a
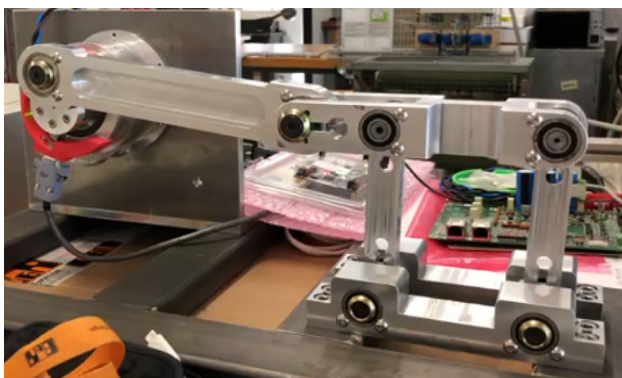
Table 2 Mechanism dimensions

	Mechanism dimensions and positions [mm]
$l_1 = |O1A|$	30
$l_2 = |AB|$	230
$l_3 = |O2C|$	120
$l_4 = |BD|$	170
$l_5 = |CD| = |O2O3|$	110
O_1	0,116.2,0
O_2	290,0,0

full rotation of the crank, the slider performs a 60-mm translation along the x-direction and a 3.8105-mm translation along the y-direction. During the nominal operating condition, the crankshaft has constant angular velocity $\omega_1 = 600$ rpm (10-Hz pushing frequency). The motor torque as function of the angular position is obtained through a rigid multi-body simulation in which friction has not been considered. From the simulation, a peak torque of $T_{m,peak} = 2.61$ Nm and an RMS torque of $T_{m,RMS} = 1.63$ Nm over a full cycle were obtained.

3 New design approach

The new design approach is based on the following steps:

1. resorting to FDM printing of CFRN/onyx for the realization of the majority of the parts of the mechanism;
2. exploiting TO so as to reduce the mass of those bulky parts that require to be stiff, keeping the geometrical dimensions as requested for the proper functioning of the mechanism.
3. replacing rigid links and traditional kinematic pairs with CJ (in particular, flexible laminas) according to the desired kinematics and range of motion: properly designed CJ, especially flexible lamina, may reach a very wide range of rotation (up to $\pm 80°$ with a good accuracy) beyond which a traditional kinematic pair is needed. To keep the kinematic compatibility with the original mechanism, the centers of rotation of the virtual joints of the PRB model must coincide with the
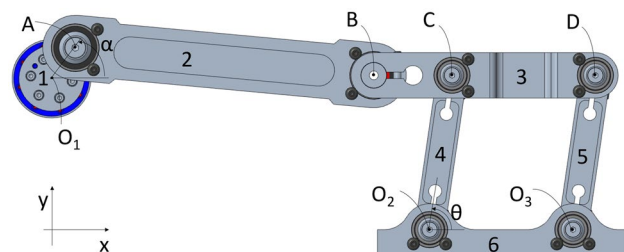

Fig. 1 Stephenson six-bar linkage prototype

Fig. 2 Six-bar linkage Stephenson mechanism schematic

real ones. Therefore, laminas of the new mechanism are longer than the actual length of the respective links;

4. dimensioning the CJ via SO to make the mechanism operating under a "resonating" condition, which enables the bidirectional transfer between link kinetic energy and CJ elastic energy, while involving the minimum power flow from/to the motor. In accordance with the PRB model, each virtual joint is accompanied by a virtual torsional spring (that is related to its flexural stiffness). If flexible lamina damping dissipation has to be accounted for, a virtual torsional damper with an appropriate damping coefficient can be added in parallel to each torsional spring of the PRB model. The CJ dimensioning problem is a dynamic optimization problem in which the virtual spring stiffnesses are the search parameters and the goal is to minimize the motor torque RMS value over a mechanism full motion cycle. For each optimization evaluation case, the lamina thickness (in the presented case of study, each lamina width, b, is kept equal to 20 mm for structural and mounting reasons) is computed from the stiffness: mass and inertia of each lamina are calculated accordingly and used in the simulation. Mass and inertia of the other mechanism components are defined during step 2 and do not change between one iteration and the other. Lagrange equation is used to obtain the motor torque as function of the virtual joint stiffnesses. Damping and friction are not considered. Since flexible lamina flexural stiffness affects its thickness and width, care must be taken to avoid buckling failure: the maximum value of the compression force acting along the longitudinal direction of each lamina must be lower than the Euler's critical load. Based on other constraints, proper rules can be implemented to limit the stiffness value range.

According to this procedure, the original mechanism undergoes the following modifications:

1. all the bearings apart from those placed in O1 and A, which perform a 360° rotation, can be replaced with CJ. In fact, joints placed in C, D, O2, and O3 rotate by ± 14.5° and joint in B rotates by ± 6.5°;
2. links 2, 4, and 5 are entirely replaced with flexible laminas with stiffness designed according to step 4. A fixed-guided model is used for laminas 4 and 5, whereas a fixed-pin model is adopted for lamina 2. The resulting PRB model is shown in Fig. 3. In order to match the virtual joints with the real joints, lamina 2 has an effective length of 282 mm, whereas laminas 4 and 5 of 140.9 mm.
3. laminas 2, 4, and 5 are printed with the higher-level carbon fiber filling CFRN (Table 2) in order to have the lower possible thickness and to be made with the lower quantity of nylon to reduce the viscous dissipation contribution. To maximize their stiffness, the crank and the
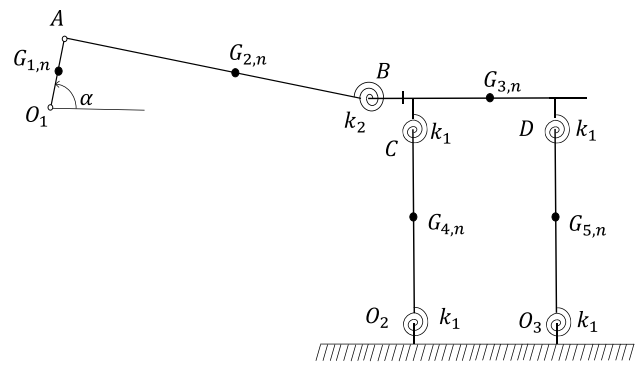

Fig. 3 Stephenson six-bar-linkage PRB model

slider are printed with higher-level carbon fiber filling CFRO. The printing concentric pattern has been used.

To proceed with the lamina SO, based on the PRB model theory [72], the virtual spring stiffnesses k_1 (for link 2) and k_2 (for link 4 and 5) are computed as follows:

$$k_1 = E_f I_2 \gamma K_\Theta / l_{2,n} \tag{1}$$

$$k_2 = 2 E_f I_4 \gamma K_\Theta / l_{4,n} \tag{2}$$

where $I_2 = b \, s_2^3/12$, $l_{2,n}$, and s_2 being the area moment of inertia, the new length and the thickness of lamina 2; $I_4 = b \, s_4^3/12$, $l_{4,n}$, and s_4 being the area moment of inertia, the new length and the thickness of laminas 4 and 5; γ and K_Θ are constants that depend on the force direction. In order to prevent mechanism failure, the Euler's critical load has to be higher than compression force $F_{2,max}$ acting on the lamina 2

$$F_{2,max} \le \pi^2 E_f I_2 / l_0^2 \tag{3}$$

where $l_0 = 0.7 \, l$ (l is the effective length for the fixed-pin beam that models lamina 2). An additional constraint is imposed on the lamina stiffness due to structural and installation reasons. Based on the authors' experience, considering the laminas length, a maximum value of 4 Nm/rad is imposed on the maximum value of stiffness. Mounting flexible laminas featuring high stiffness would indeed require design measures that significantly complicate the system, increasing the component inertia which completely nullifies the contribution of TO on motor torque reduction.

The redesigned compliant mechanism resulting from the procedure is shown in Fig. 4.

4 Results and experimental analysis

From the procedure, the optimal value of the stiffnesses $k_{1,opt}$ and $k_{2,opt}$ is found to be 4 Nm/rad and 2.63 Nm/rad, respectively. The correspondent minimum motor torque

Fig. 4 Stephenson six-bar-linkage PRB model

RMS value is found to be $T_{m,RMS} = 0.0283$ Nm (peak value $T_{m,peak} = 0.0590$ Nm), with a reduction with respect to the original mechanism RMS motor torque by 98% (97% reduction on the peak value). A prototype of the mechanism has been built (Fig. 5): the mass of the new mechanism components is shown in Table 3 (with a reduction up to 93% with respect to the original mechanism component mass). To avoid fiber exposure on the outer surface and to have the higher quality surface finish and accuracy of the unreinforced nylon, the first and last layers of the printed part are forced, by the MarkTwo software, to be made of matrix material only. Given the lamina stiffness values, the correspondent thickness is computed exploiting Eqs. (1) and (2): the equivalent flexural modulus for composite material is evaluated according to classical lamination theory [99] considering a lamina with the inner CFRN layers and the external layers made of nylon (mechanical characteristics are listed in Table 1). It is worth noting that the exact value of the flexural modulus (and thus the stiffness) cannot be achieved due to the 3D printing manufacturing process resolution (a minimum layer thickness of only 0.125 mm is achievable when fiber reinforcement is employed). In fact, the nearest thickness value to $k_{1,opt}$ that can be achieved is 4.29 Nm/rad with a thickness of 2 mm (13 CFRN inner layers and 2 0.125 mm external unreinforced Nylon layers) and to $k_{2,opt}$ is 2.37 Nm/rad

Table 3 Link mass reduction

	Crank	**Rod**	**Slider**	**Rocker**
Original [kg]	0.076	0.322	0.401	0.076
New [kg]	0.045	0.084	0.151	0.005
Reduction [%]	40.8	73.9	62	93

with a thickness of 1.125 mm (7 CFRN inner layers and 2 0.125 mm external unreinforced nylon layers).

Two experimental tests (Fig. 6) have been conducted to assess the real value of the stiffnesses $k_{1,real}$ and $k_{2,real}$. The flexible lamina Young modulus real value is obtained through the evaluation of the cantilever beam first flexural vibration mode according to the following relation [100]:

$$p_q = (r_q l)^2 \sqrt{\frac{E_f I}{ml^4}} \qquad (4)$$

where $q = 1$ (for the first mode), $r_q l = 1.875$, m is the mass (15.2 g, 4.8 g, and 4.8 g for laminas 2, 4, and 5, respectively), whereas l and I are the length and the area moment of inertia of the lamina. In fact, unlike the direct measurement of the lamina stiffness, the free vibration deflection of a flexible lamina can be easily measured with a laser position sensor, thus providing high reliable data about the frequency. Stiffnesses $k_{1,real}$ and $k_{2,real}$ are successively computed introducing the respective Young modulus in Eqs. (1) and (2) (to reduce the source of error, the quantity $E_f I$ is computed from Eq. (4) and inserted in Eqs. (1) and (2)).

During the test, a displacement is imposed to the tip of the lamina and subsequently removed. The free vibration deflection of the lamina is registered. A Panasonic HG-C1050 laser sensor (range ± 15 mm, resolution 30 μm, sampling frequency 666.67 Hz) is used to register the motion. The first flexural vibration frequency is found to be 23.08 Hz, 41.38 Hz, and 37.74 Hz for laminas 2, 4, and 5, respectively. It is worth noting that for laminas 4 and 5, the tested natural frequency vibration mode is not related to the one that occurs during the nominal functioning condition in which

Fig. 5 Prototype of the redesigned mechanism

Fig. 6 Set-up used to test the cantilever beam to find the lamina Young modulus

Fig. 7 Motor torque as function of the angular position obtained for the original mechanism (red experimental and blue simulated)

laminas are in a fixed-guided constraint condition (no rotation occurs on the lamina tip).

The real value of the stiffnesses are $k_{1,real} = 4.58$ Nm/rad, $k_{24,real} = 3.08$ Nm/rad, and $k_{25,real} = 2.56$ Nm/rad: the small discrepancy with the expected values ($k_{1,opt} = 4.29$ Nm/rad and $k_2 = 2.37$ Nm/rad) is caused by the MarkForged manufacturing poor accuracy. The real lamina thickness was measured and the following values are found: $s_2 = 2.373 \pm 0.147$ mm, $s_4 = 1.43 \pm 0.02$ mm, and $s_5 = 1.275 \pm 0.05$ mm. The mechanism has been simulated with the real stiffness values obtained from the tests (different from the optimal ones): motor RMS and peak torque values are found to be $T_{m,RMS} = 0.0287$ Nm and $T_{m,peak} = 0.0597$ Nm.

An experimental campaign has been conducted to compare the real performances of the mechanisms designed according to the two different approaches. The following values of the motor torque are registered: for the original mechanism (Fig. 7), the RMS and peak values are 1.78 Nm and 2.84 Nm, respectively, whereas for the redesigned one (Fig. 8) are 0.0509 Nm and 0.1114 Nm, respectively (97% and 96% reduction on the RMS and peak motor torques). The maximum difference between the ideal and corresponding experimental motor torques over a cycle is 0.23 Nm for the original mechanism and 0.08 Nm for the redesigned one, meaning that the overall contribution of the dissipation due to friction and damping is reduced by 65%. Moreover, the tests were conducted for different values of the crankshaft angular velocity (Fig. 9): 100 rpm, 200 rpm, 300 rpm, 400 rpm, 600 rpm, 700 rpm, 800 rpm, and 900 rpm. The motor torque RMS and peak minimum value are obtained for 600-rpm angular velocity. The simulated (with real stiffness
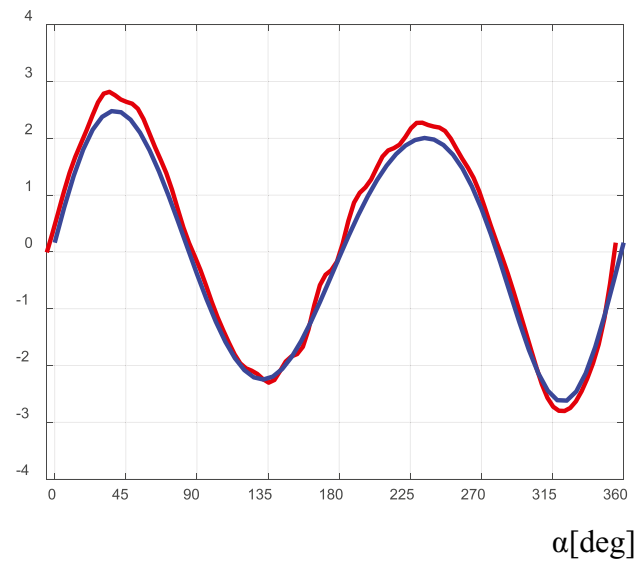
values) and experimental RMS and peak values as a function of the crankshaft angular velocity are shown in Fig. 9. Experimental required motor torque as function of the crankshaft angular position is reported in Fig. 10 for the various considered speeds.

Two laser sensors Panasonic HG-C1050 and Panasonic HL-GI112-A-C5 (range ± 60 mm, resolution 8 µm, sampling rate 1000 µs) have been used to measure the motion trajectory of the slider for the redesigned mechanism at 600 rpm angular velocity: the lasers are fixed to the frame and register
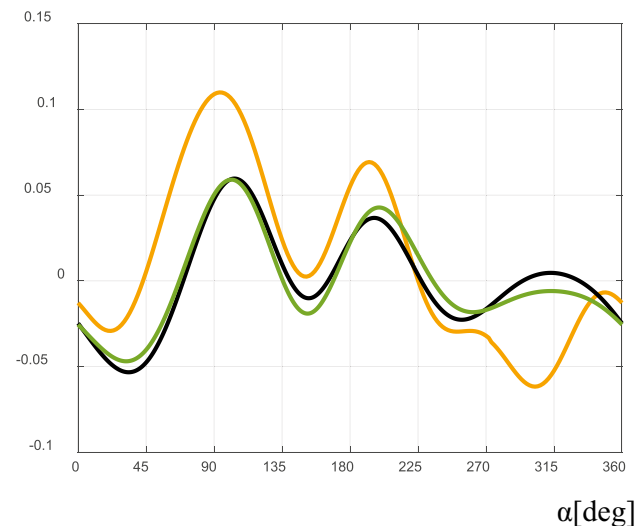

Fig. 8 Motor torque as function of the angular position obtained for the redesinged mechanism (orange experimental, green simulated with optimal stiffness values and black simulated with real stiffness values)
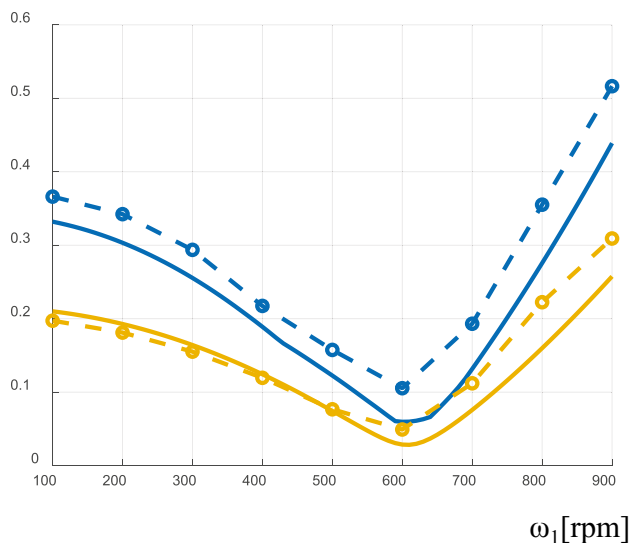
Fig. 9 Simulated (continuous line) and experimental (dashed line with circle markers) RMS (yellow) and peak (blue) values as a function of the crankshaft angular position
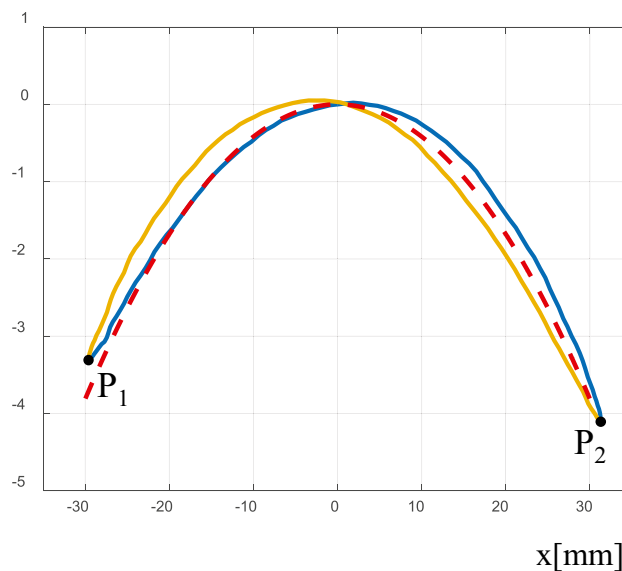

Fig. 11 Slider motion trajectory (dashed red is the ideal trajectory and yellow (backward direction) and blue (forward direction) is the measured one) in the x–y plane

the distance of a planar surface of the slider. Twenty consecutive cycles of the same slider motion trajectory were registered: its mean value is shown in Fig. 11. The measure is affected by the error due to possible rotation of the slider around the z axis, which is supposed to be small. When the slider reaches the extremities, lasers recorded a translation of -4.12 mm and -31.31 mm ($\alpha = 180°$, point P_1 in Fig. 11) along x and y directions, respectively, and -3.30 mm and 29.49 mm ($\alpha = 0°$, point P_2 in Fig. 11) with respect to the home position. The slider motion trajectory of the flexible mechanism in the x–y plane fits fairly well the ideal trajectory (dashed red line in Figs. 11 and 12). However, due to variation of the internal force direction, during the backward

motion ($\alpha = 0$–$180°$; blue line in Figs. 11 and 12) the slider follows a similar but not identical path with respect to the one performed in the forward motion ($\alpha = 180$–$360°$; yellow line in Figs. 11 and 12). The maximum value of the distance between the two trajectories for a given x is 0.67 mm and occurs for $x = -24.6$ mm (forward direction). For the considered motion trajectory cycles, the obtained position repeatability is 0.1 mm. The maximum value of the
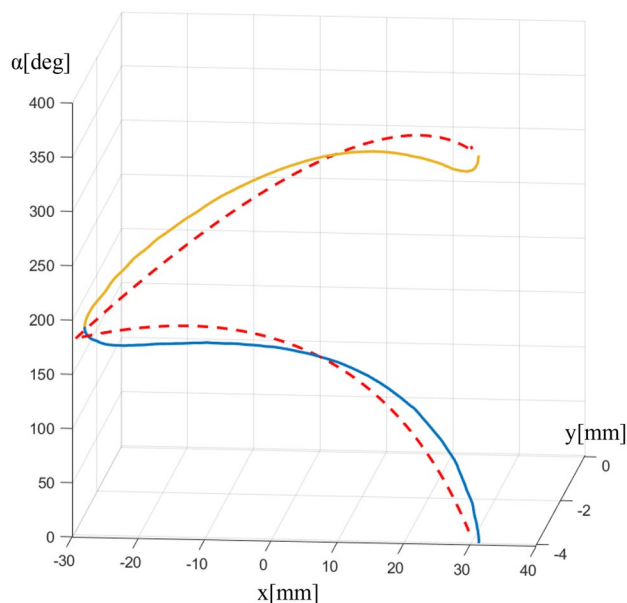

Fig. 10 Experimental motor torque as a function of the angular position α at several values of crankshaft angular velocity

Fig. 12 Slider motion trajectory (dashed red is the ideal trajectory and yellow (backward direction) and blue (forward direction) is the measured one) as a function of x, y, and α
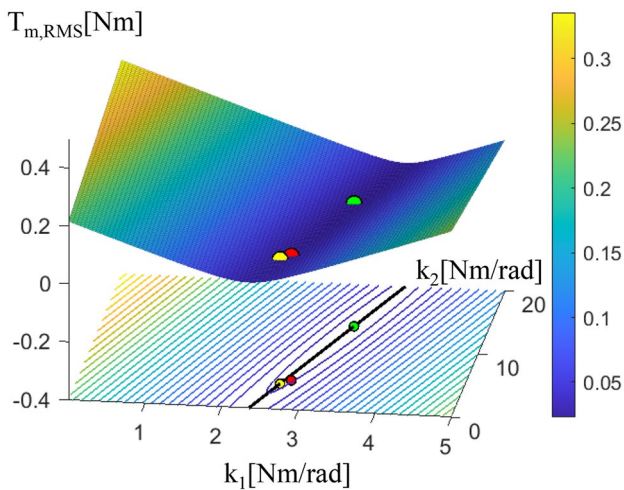
Fig. 13 RMS motor torque as function of stiffnesses k_1 and k_2. The yellow point is the optimal condition obtained from the procedure, red point is the real working condition, and green point is the optimal condition when limits on the stiffness range are not applied. The black line identifies the set of optimal conditions

distance between the two trajectories for a given α (Fig. 12) is 7.26 mm and occurs when $\alpha = 34.95°$.

Since lamina 2 stiffness value reaches the upper limit imposed during the SO procedure, the limitation on the final optimal result due to the permissible stiffness range is investigated. Figure 13 shows the RMS motor torque as function of the stiffnesses k_1 and k_2: the $T_{m,RMS}$ reaches its minimum at 0.0229 Nm (peak value $T_{m,peak} = 0.0444$ Nm) with a reduction of 99% (98% reduction on the peak value) with respect to the correspondent value obtained from the original mechanism simulation and occurs when k_1 and k_2 are 13.43 Nm/rad and 3.26 Nm/rad (green point in Fig. 13), respectively. The set of optimal solutions is identified by the black line in Fig. 13. Although the real stiffnesses (red point in Fig. 13) differ by up to 30% from the optimal values (yellow point in Fig. 13), only a negligible difference (0.004 Nm) results in the motor torque RMS value.

5 Conclusion

In this paper, a new approach to design mechanisms for automated machinery has been proposed that proved very successful in the reduction of motor torque requirements and also demonstrated good capabilities in predicting mechanism behavior. Three main effects contribute to decrease the required motor torque.

1. Introduction of flexible laminas, which brings elastic energy storing/releasing components that make the mechanism work in a "resonant" condition.

2. The combined usage of flexible laminas and TO, which eliminates components (in this case, twelve ball bearings are removed) and reduces link masses (from 40 to 93%), thereby diminishing inertial actions (the prevailing loadings in automated machinery mechanisms). Mass reduction is also obtained thanks to the employed AMT materials: CFRN and CFRO indeed feature lower density than aluminium alloy, despite maintaining the other high-performance mechanical characteristics.

3. Significant reduction of friction is achieved through the removal of ball bearings. The viscous dissipation caused by the flexible laminas is indeed lower than the friction losses present in ball bearings.

The replacement of ball bearings with flexible laminas also simplifies mechanical design and removes backlash. Moreover, relatively high repeatability is achieved, which is of paramount importance in automated machinery. However, the precision of the slider motion trajectory is limited due to the following two main reasons.

1. Lamina deformation is affected by the direction of the loads (in particular, of the inertial loads), which makes the trajectory of the slider during the forward motion be different than the one in the backward motion.

2. The adoption of the considered PRB model for system design. To increase the precision, more advanced PRB models or FEA-based methods should be used; the latter however drastically increasing the time required for design completion. Nonetheless, the design procedure proposed here is more time consuming than the standard one. In fact, surface refining phase required by TO is a long process that depends on the designer expertise.

In combination with the proposed design approach, 3D printing proved to be an effective manufacturing process to match the necessary mechanical characteristics with the requested component shape. Poor planarity and precision of the fabrication (resulting in up to 30% higher stiffness values) did not have a major influence on the motor torque results.

Although an optimal solution is achieved, a non-zero motor torque that varies with the mechanism position is still present. This is mostly due to the mismatch between the system free-vibration trajectory and the motion imposed by the constant velocity of the crankshaft. To solve this issue, future research will include motor trajectory optimization in the design procedure.

Data availability Not applicable.

Code availability Not applicable.

Declarations

Ethics approval Not applicable.

Consent to participate Not applicable.

Consent for publication Not applicable.

Competing interests The authors declare no competing interests.

References

1. Berselli G, Bilancia P, Luzi L (2020) Project-based learning of advanced CAD/CAE tools in engineering education. Int J Interact Des Manuf 14(3)
2. Chang KH (2014) Design theory and methods using CAD/CAE: the computer aided engineering design series
3. Vergnano A, Berselli G, Pellicciari M (2017) Parametric virtual concepts in the early design of mechanical systems: a case study application. Int J Interact Des Manuf 11(2)
4. Gujarathi GP, Ma YS (2011) Parametric CAD/CAE integration using a common data model. J Manuf Syst 30(3). https://doi.org/10.1016/j.jmsy.2011.01.002
5. Cao BW, Chen JJ, Huang ZG, Zheng Y (2009) CAD/CAE integration framework with layered software architecture. https://doi.org/10.1109/CADCG.2009.5246866
6. Penoyer JA, Burnett G, Fawcett DJ, Liou SY (2000) Knowledge based product life cycle systems: principles of integration of KBE and C3P. CAD Comput Aided Des 32(5). https://doi.org/10.1016/S0010-4485(00)00014-2
7. Aziz ES, Chassapis C (2002) Knowledge-based geometry generation for spur and helical gears. Concurr Eng Res Appl 10(3). https://doi.org/10.1177/106329302761689160
8. Chapman CB, Pinfold M (1999) Design engineering - a need to rethink the solution using knowledge based engineering. Knowl-Based Syst 12(5–6). https://doi.org/10.1016/S0950-7051(99)00013-1
9. Anumba CJ (1996) Functional integration in CAD systems. Adv Eng Softw 25(2–3). https://doi.org/10.1016/0965-9978(95)00102-6
10. Shephard MS, Beall MW, O'Bara RM, Webster BE (2004) Toward simulation-based design. Finite Elem Anal Des 40(12). https://doi.org/10.1016/j.finel.2003.11.004
11. Yan Z, Jiang Z (2009) Research on the integrated design of dual mass flywheel CAD/CAE/CAM. Key Eng Mater 407–408. https://doi.org/10.4028/www.scientific.net/KEM.407-408.169
12. Sun W, Ma Q, Chen S (2009) A framework for automated finite element analysis with an ontology-based approach. J Mech Sci Technol 23(12). https://doi.org/10.1007/s12206-009-1005-0
13. Foucault G, Cuillière JC, François V, Léon JC, Maranzana R (2008) Adaptation of CAD model topology for finite element analysis. CAD Comput Aided Des 40(2). https://doi.org/10.1016/j.cad.2007.10.009
14. Xu XY, Wang YY (2002) Multi-model technology and its application in the integration of CAD/CAM/CAE. J Mater Process Technol 129(1–3). https://doi.org/10.1016/S0924-0136(02)00639-8
15. Xu B, Chen N (2009) An integrated method of CAD, CAE and multi-objective optimization. https://doi.org/10.1109/CAIDCD.2009.5375416
16. Sangolkar RN, Kshirsagar VP (2015) Modelling and analysis of industrial belt conveyor system using creo parametric and Ansys software. Int J Tech Res Appl 3(4)
17. Ravikiran M, Prasad SA, Srujana V, Abhhimanyu KSS (2021) Weight optimization of piston using CREO parametric and ANSYS. IOP Conf Ser Mater Sci Eng 1057. https://doi.org/10.1088/1757-899x/1057/1/012047
18. Luzi L, Quercioli G, Pucci R, Bocchieri G, Vertechy R, Berselli G (2020) Additively manufactured continuous fibre-reinforced thermoplastics for mechanisms subjected to predominant inertial load: a case study. https://doi.org/10.1115/smasis2020-2320
19. Luzi L et al (2021) 3D printed resonant compliant mechanism to reduce motor torque requirements of machines with cyclic operation. https://doi.org/10.1115/smasis2021-68293
20. Wang L, Liu J, Chen L (2017) Simulation comparison between PTC/Creo and professional CAE software. DEStech Trans Eng Technol Res (icmme). https://doi.org/10.12783/dtetr/icmme2017/9041
21. Park HS, Dang XP (2010) Structural optimization based on CADCAE integration and metamodeling techniques. CAD Comput Aided Des 42(10). https://doi.org/10.1016/j.cad.2010.06.003
22. Li C, Kim IY, Jeswiet J (2015) Conceptual and detailed design of an automotive engine cradle by using topology, shape, and size optimization. Struct Multidiscipl Optim 51(2). https://doi.org/10.1007/s00158-014-1151-6
23. Shieh RC (1994) Massively parallel structural design using stochastic optimization and mixed neuralnet/finite element analysis methods. Comput Syst Eng 5(4–6). https://doi.org/10.1016/0956-0521(94)90026-4
24. Kikuchi KSN (2013) Layout optimization using the homogenization method. Optim Large Struct Syst 231:157
25. Eschenauer HA, Schumacher A, Vietor T (1993) Decision makings for initial designs made of advanced materials. Topol Des Struct. https://doi.org/10.1007/978-94-011-1804-0_33
26. Xie YM, Steven GP (1994) Optimal design of multiple load case structures using an evolutionary procedure. Eng Comput 11(4). https://doi.org/10.1108/02644409410799290
27. Schäfer C, Finke E (2008) Shape optimisation by design of experiments and finite element methods-an application of steel wheels. Struct Multidiscipl Optim 36(5). https://doi.org/10.1007/s00158-007-0183-6
28. Bendsøe MP, Kikuchi N (1988) Generating optimal topologies in structural design using a homogenization method. Comput Methods Appl Mech Eng 71(2). https://doi.org/10.1016/0045-7825(88)90086-2

29. Turner BN, Strong R, Gold SA (2014) A review of melt extrusion additive manufacturing processes: I. Process design and modeling. Rapid Prototyp J 20(3). https://doi.org/10.1108/RPJ-01-2013-0012

30. Murr LE et al (2012) Metal fabrication by additive manufacturing using laser and electron beam melting technologies. J Mater Sci Technol 28(1). https://doi.org/10.1016/S1005-0302(12)60016-4

31. Gibson I, Rosen DW, Stucker B (2010) Additive manufacturing technologies: rapid prototyping to direct digital manufacturing. https://doi.org/10.1007/978-1-4419-1120-9

32. Zhu J, Zhou H, Wang C, Zhou L, Yuan S, Zhang W (2021) A review of topology optimization for additive manufacturing: status and challenges. Chin J Aeronaut 34(1). https://doi.org/10.1016/j.cja.2020.09.020

33. Bendsøe MP (1989) Optimal shape design as a material distribution problem. Struct Optim 1(4). https://doi.org/10.1007/BF01650949

34. Zhou M, Rozvany GIN (1991) The COC algorithm, part II: topological, geometrical and generalized shape optimization. Comput Methods Appl Mech Eng 89(1–3). https://doi.org/10.1016/0045-7825(91)90046-9

35. Mlejnek HP (1992) Some aspects of the genesis of structures. Struct Optim 5(1–2). https://doi.org/10.1007/BF01744697

36. Allaire G, Jouve F, Toader AM (2004) Structural optimization using sensitivity analysis and a level-set method. J Comput Phys 194(1). https://doi.org/10.1016/j.jcp.2003.09.032

37. Allaire G, Jouve F, Toader AM (2002) A level-set method for shape optimization. C R Math 334(12). https://doi.org/10.1016/S1631-073X(02)02412-3

38. Wang MY, Wang X, Guo D (2003) A level set method for structural topology optimization. Comput Methods Appl Mech Eng 192(1–2). https://doi.org/10.1016/S0045-7825(02)00559-5

39. van Dijk NP, Maute K, Langelaar M, van Keulen F (2013) Level-set methods for structural topology optimization: a review. Struct Multidiscipl Optim 48(3). https://doi.org/10.1007/s00158-013-0912-y

40. Sigmund O, Maute K (2013) Topology optimization approaches: a comparative review. Struct Multidiscipl Optim 48(6). https://doi.org/10.1007/s00158-013-0978-6

41. Liu S, Li Q, Liu J, Chen W, Zhang Y (2018) A realization method for transforming a topology optimization design into additive manufacturing structures. Engineering 4(2). https://doi.org/10.1016/j.eng.2017.09.002

42. Liu S, Hu R, Li Q, Zhou P, Dong Z, Kang R (2014) Topology optimization-based lightweight primary mirror design of a large-aperture space telescope. Appl Opt 53(35). https://doi.org/10.1364/ao.53.008318

43. Harzheim L, Graf G (2006) A review of optimization of cast parts using topology optimization. Struct Multidiscipl Optim 31(5). https://doi.org/10.1007/s00158-005-0554-9

44. Lee AY, An J, Chua CK (2017) Two-way 4D printing: a review on the reversibility of 3D-printed shape memory materials. Engineering 3(5). https://doi.org/10.1016/J.ENG.2017.05.014

45. Lu B, Li D, Tian X (2015) Development trends in additive manufacturing and 3D printing. Engineering 1(1). https://doi.org/10.15302/J-ENG-2015012

46. Han P (2017) Additive design and manufacturing of jet engine parts. Engineering 3(5). https://doi.org/10.1016/J.ENG.2017.05.017

47. Hopkinson N, Hague RJM, Dickens PM (2006) Rapid manufacturing: an industrial revolution for the digital age. https://doi.org/10.1002/0470033991

48. Gebisa AW, Lemu HG (2017) A case study on topology optimized design for additive manufacturing. IOP Conf Ser Mater Sci Eng 276(1). https://doi.org/10.1088/1757-899X/276/1/012026

49. Liu J et al (2018) Current and future trends in topology optimization for additive manufacturing. Struct Multidiscipl Optim 57(6). https://doi.org/10.1007/s00158-018-1994-3

50. Horn TJ, Harrysson OLA (2012) Overview of current additive manufacturing technologies and selected applications. Sci Prog 95(3). https://doi.org/10.3184/003685012X13420984463047

51. Thompson MK et al (2016) Design for additive manufacturing: trends, opportunities, considerations, and constraints. CIRP Ann Manuf Technol 65(2). https://doi.org/10.1016/j.cirp.2016.05.004

52. Kruth JP, Leu MC, Nakagawa T (1998) Progress in additive manufacturing and rapid prototyping. CIRP Ann Manuf Technol 47(2). https://doi.org/10.1016/S0007-8506(07)63240-5

53. Levy GN, Schindel R, Kruth JP (2003) Rapid manufacturing and rapid tooling with layer manufacturing (LM) technologies, state of the art and future perspectives. CIRP Ann Manuf Technol 52(2). https://doi.org/10.1016/S0007-8506(07)60206-6

54. Tekinalp HL et al (2014) Highly oriented carbon fiber-polymer composites via additive manufacturing. Compos Sci Technol 105. https://doi.org/10.1016/j.compscitech.2014.10.009

55. Shofner ML, Lozano K, Rodríguez-Macías FJ, Barrera EV (2003) Nanofiber-reinforced polymers prepared by fused deposition modeling. J Appl Polym Sci 89(11). https://doi.org/10.1002/app.12496

56. Gray RW IV, Baird DG, Bøhn JH (1998) Thermoplastic composites reinforced with long fiber thermotropic liquid crystalline polymers for fused deposition modeling. Polym Compos 19(4). https://doi.org/10.1002/pc.10112

57. Gray RW IV, Baird DG, Bøhn JH (1998) Effects of processing conditions on short TLCP fiber reinforced FDM parts. Rapid Prototyp J 4(1). https://doi.org/10.1108/13552549810197514

58. Zhong W, Li F, Zhang Z, Song L, Li Z (2001) Short fiber reinforced composites for fused deposition modeling. Mater Sci Eng A 301(2). https://doi.org/10.1016/S0921-5093(00)01810-4

59. Shubhra QTH, Alam AKMM, Quaiyyum MA (2013) Mechanical properties of polypropylene composites: a review. J Thermoplast Compos Mater 26(3). https://doi.org/10.1177/0892705711428659

60. Kinet D, Mégret P, Goossen KW, Qiu L, Heider D, Caucheteur C (2014) Fiber Bragg grating sensors toward structural health monitoring in composite materials: challenges and solutions. Sensors (Switzerland) 14(4). https://doi.org/10.3390/s140407394

61. Gay D, Hoa SV, Tsai SW (2002) Composite materials: design and applications

62. Dickson AN, Barry JN, McDonnell KA, Dowling DP (2017) Fabrication of continuous carbon, glass and Kevlar fibre reinforced polymer composites using additive manufacturing. Addit Manuf 16. https://doi.org/10.1016/j.addma.2017.06.004

63. Hart RJ, Patton EG, Sapunkov O (2018) Characterization of continuous fiber-reinforced composite materials manufactured via fused filament fabrication. ARMY TANK AUTOMOTIVE RESEARCH DEVELOPMENT AND ENGINEERING CENTER WARREN MI WARREN United States

64. Goh GD et al (2018) Characterization of mechanical properties and fracture mode of additively manufactured carbon fiber and glass fiber reinforced thermoplastics. Mater Des 137. https://doi.org/10.1016/j.matdes.2017.10.021

65. Blok LG, Longana ML, Yu H, Woods BKS (2018) An investigation into 3D printing of fibre reinforced thermoplastic composites. Addit Manuf 22. https://doi.org/10.1016/j.addma.2018.04.039

66. Ghebretinsae F, Mikkelsen O, Akessa AD (2019) Strength analysis of 3D printed carbon fibre reinforced thermoplastic using experimental and numerical methods. IOP Conf Ser Mater Sci Eng 700(1). https://doi.org/10.1088/1757-899X/700/1/012024

67. Dutra TA, Ferreira RTL, Resende HB, Guimarães A (2019) Mechanical characterization and asymptotic homogenization of 3D-printed continuous carbon fiber-reinforced thermoplastic.

J Braz Soc Mech Sci Eng 41(3). https://doi.org/10.1007/s40430-019-1630-1

68. van der Klift F, Koga Y, Todoroki A, Ueda M, Hirano Y, Matsuzaki R (2016) 3D printing of continuous carbon fibre reinforced thermoplastic (CFRTP) tensile test specimens. Open J Compos Mater 06(01). https://doi.org/10.4236/ojcm.2016.61003

69. Poissenot-Arrigoni B, Scheyer A, Anton SR (2017) Determination of orthotropic mechanical properties of 3D printed parts for structural health monitoring. Sens Smart Struct Technol Civil Mech Aerosp Syst 10168. https://doi.org/10.1117/12.2260397

70. Berselli G, Guerra A, Vassura G, Andrisano AO (2014) An engineering method for comparing selectively compliant joints in robotic structures. IEEE/ASME Trans Mechatron 19(6). https://doi.org/10.1109/TMECH.2014.2315508

71. Gouker RM, Gupta SK, Bruck HA, Holzschuh T (2006) Manufacturing of multi-material compliant mechanisms using multi-material molding. Int J Adv Manuf Technol 30(11–12). https://doi.org/10.1007/s00170-005-0152-4

72. Howell LL, Magleby SP, Olsen BM (2013) Handbook of compliant mechanisms. https://doi.org/10.1002/9781118516485

73. Merriam EG, Howell LL (2016) Lattice flexures: geometries for stiffness reduction of blade flexures. Precis Eng 45. https://doi.org/10.1016/j.precisioneng.2016.02.007

74. Trease BP, Moon YM, Kota S (2005) Design of large-displacement compliant joints. J Mech Des Trans ASME 127(4). https://doi.org/10.1115/1.1900149

75. Guo J, Lee KM (2013) Compliant joint design and flexure finger dynamic analysis using an equivalent pin model. Mech Mach Theory 70. https://doi.org/10.1016/j.mechmachtheory.2013.08.001

76. Qiu J, Lang JH, Slocum AH (2004) A curved-beam bistable mechanism. J Microelectromech Syst 13(2). https://doi.org/10.1109/JMEMS.2004.825308

77. She Y, Su HJ, Lai C, Meng D (2016) Design and prototype of a tunable stiffness arm for safe human-robot interaction. Proc ASME Des Eng Tech Conf 5B–2016. https://doi.org/10.1115/DETC2016-59523

78. She Y, Su HJ, Meng D, Song S, Wang J (2018) Design and modeling of a compliant link for inherently safe corobots. J Mech Robot 10(1). https://doi.org/10.1115/1.4038530

79. Kang BH, Wen JTY, Dagalakis NG, Gorman JJ (2005) Analysis and design of parallel mechanisms with flexure joints. IEEE Trans Robot 21(6). https://doi.org/10.1109/TRO.2005.855989

80. Kota S, Joo J, Li Z, Rodgers SM, Sniegowski J (2001) Design of compliant mechanisms: applications to MEMS. Analog Integr Circuits Signal Process 29(1–2). https://doi.org/10.1023/A:1011265810471

81. Monkman GJ, Hesse S, Steinmann R, Schunk H (2007) Robot Grippers. https://doi.org/10.1002/9783527610280

82. Berselli G, Vertechy R, Babič M, Parenti Castelli V (2013) Dynamic modeling and experimental evaluation of a constant-force dielectric elastomer actuator. J Intell Mater Syst Struct 24(6). https://doi.org/10.1177/1045389X12457251

83. Kota S, Lu KJ, Kreiner Z, Trease B, Arenas J, Geiger J (2005) Design and application of compliant mechanisms for surgical tools. J Biomech Eng 127(6). https://doi.org/10.1115/1.2056561

84. Lourdes Thomas T, Kalpathy Venkiteswaran V, Ananthasuresh GK, Misra S (2021) Surgical applications of compliant mechanisms: a review. J Mech Robot 13(2). https://doi.org/10.1115/1.4049491

85. Palli G, Pirozzi S (2011) Miniaturized optical-based force sensors for tendon-driven robots. https://doi.org/10.1109/ICRA.2011.5979970

86. Guérinot AE, Magleby SP, Howell LL, Todd RH (2005) Compliant joint design principles for high compressive load situations. J Mech Des Trans ASME 127(4). https://doi.org/10.1115/1.1862677

87. Lobontiu N, Garcia E (2005) Circular-hinge line element for finite element analysis of compliant mechanisms. J Mech Des Trans ASME 127(4). https://doi.org/10.1115/1.1825046

88. Howell LL, Midha A (1994) A method for the design of compliant mechanisms with small-length flexural pivots. J Mech Des Trans ASME 116(1). https://doi.org/10.1115/1.2919359

89. Howell LL, Midha A, Norton TW (1996) Evaluation of equivalent spring stiffness for use in a pseudo-rigid-body model of large-deflection compliant mechanisms. J Mech Des Trans ASME 118(1). https://doi.org/10.1115/1.2826843

90. Ma F, Chen G (2016) Modeling large planar deflections of flexible beams in compliant mechanisms using chained beam-constraint-model. J Mech Robot 8(2). https://doi.org/10.1115/1.4031028

91. Turkkan OA, Su HJ (2017) A general and efficient multiple segment method for kinetostatic analysis of planar compliant mechanisms. Mech Mach Theory 112. https://doi.org/10.1016/j.mechmachtheory.2017.02.010

92. Yu YQ, Feng ZL, Xu QP (2012) A pseudo-rigid-body 2R model of flexural beam in compliant mechanisms. Mech Mach Theory 55. https://doi.org/10.1016/j.mechmachtheory.2012.04.005

93. Su HJ (2008) A load independent pseudo-rigid-body 3R model for determining large deflection of beams in compliant mechanisms. Proc ASME Des Eng Tech Conf 2(Parts A and B). https://doi.org/10.1115/DETC2008-49041

94. She Y, Meng D, Su HJ, Song S, Wang J (2018) Introducing mass parameters to pseudo–rigid–body models for precisely predicting dynamics of compliant mechanisms. Mech Mach Theory 126. https://doi.org/10.1016/j.mechmachtheory.2018.04.005

95. Caminero MA, Chacón JM, García-Moreno I, Reverte JM (2018) Interlaminar bonding performance of 3D printed continuous fibre reinforced thermoplastic composites using fused deposition modelling. Polym Test 68. https://doi.org/10.1016/j.polymertesting.2018.04.038

96. Caminero MA, Chacón JM, García-Moreno I, Rodríguez GP (2018) Impact damage resistance of 3D printed continuous fibre reinforced thermoplastic composites using fused deposition modelling. Compos Part B Eng 148. https://doi.org/10.1016/j.compositesb.2018.04.054

97. Melenka GW, Cheung BKO, Schofield JS, Dawson MR, Carey JP (2016) Evaluation and prediction of the tensile properties of continuous fiber-reinforced 3D printed structures. Compos Struct 153. https://doi.org/10.1016/j.compstruct.2016.07.018

98. Yu T, Zhang Z, Song S, Bai Y, Wu D (2019) Tensile and flexural behaviors of additively manufactured continuous carbon fiber-reinforced polymer composites. Compos Struct 225. https://doi.org/10.1016/j.compstruct.2019.111147

99. Reddy JN (2003) Mechanics of laminated composite plates and shells. https://doi.org/10.1201/b12409

100. Chun KR (1972) Free vibration of a beam with one end spring-hinged and the other free. J Appl Mech Trans ASME 39(4). https://doi.org/10.1115/1.3422854